FRONTIERS OF PHYSICS

TOPICAL REVIEW
Volume 18 / Issue 6 / 63602 / 2023

# Recent review of surface plasmons and plasmonic hot electron effects in metallic nanostructures

Hao Zhang[1,2,3], Mohsin Ijaz[1,2,3,†], Richard J. Blaikie[1,2,3,‡]

1 Dodd-Walls Centre for Photonic and Quantum Technologies, Dunedin, New Zealand
2 MacDiarmid Institute for Advanced Materials and Nanotechnology, Wellington, New Zealand
3 Department of Physics, University of Otago, Dunedin 9016, New Zealand
Corresponding authors. E-mail: †mohsin.ijaz@otago.ac.nz, ‡richard.blaikie@otago.ac.nz

Received May 15, 2023; accepted June 20, 2023

## ABSTRACT

Plasmonic resonators are widely used for the manipulation of light on subwavelength scales through the near-field electromagnetic wave produced by the collective oscillation of free electrons within metallic systems, well known as the surface plasmon (SP). The non-radiative decay of the surface plasmon can excite a plasmonic hot electron. This review article systematically describes the excitation progress and basic properties of SPs and plasmonic hot electrons according to recent publications. The extraction mechanism of plasmonic hot electrons via Schottky conjunction to an adjacent semiconductor is also illustrated. Also, a calculation model of hot electron density is given, where the efficiency of hot-electron excitation, transport and extraction is discussed. We believe that plasmonic hot electrons have a huge potential in the future development of optoelectronic systems and devices.

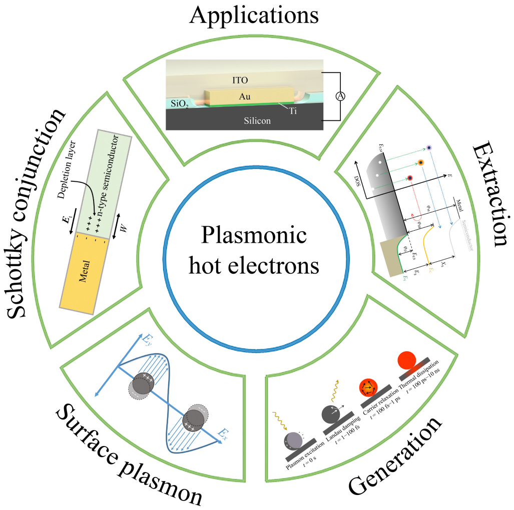

**Keywords** surface plasmon, plasmonic hot electrons, plasmonic resonators, electron–electron scattering, Schottky conjunctions, nanophotonics

## Contents

Higher Education Press

https://doi.org/10.1007/s11467-023-1328-9

## 1 Surface plasmons

The interaction of incident light with free electrons distributed on a metal surface, leading to the collective oscillation of the free electrons can create what is called a surface plasmon [1]. Surface plasmons (SPs) can produce electric fields which are confined in a very small mode volume, resulting in the near-field enhancement of incident light [2]. Moreover, SP resonance frequencies can be adjusted by changing the shape and size of metal nanostructures [3]. Therefore, SPs provide a promising approach to the flexible manipulation of light at subwavelength scale. There are various metals commonly used for plasmonics like Au, Ag, Cu, Al and others. Among all plasmonic metals, Ag is the optimum choice due to highest quality factor in the visible and near-infrared wavelength range, being attributed to its lowest loss [4]. According to whether they are propagating or not, SPs are divided into two types: Surface Plasmon Polaritons (SPPs) which is also called Propagating Surface Plasmons (PSPs), and Localized Surface Plasmon Resonances (LSPRs) as shown in Fig. 1 [5–7]. The application of SPs has been extended to a wide range of important fields such as medical science [8–10], energy [11–15], lasing [16], display [17], sensor [18–24], imaging [25, 26], cloaking [27], surface-enhanced Raman scattering (SERS) [28, 29], nonlinear optics [30–34], laser-plasmonic lithography [35, 36] and others.

### 1.1 Surface Plasmon Polaritons (SPPs)

### 1.1.1 Overview

Figure 2(a) presents a charge distribution schematic for SPPs on a planar metal surface. Under appropriate illumination, the excitation of SPPs causes the alternative distribution of positive and negative charges along the metal surface giving rise to forward-propagating energy, with decay caused by metallic loss or others [37].

Collective oscillation can excite electric fields on both sides of the interface, leading to enhancement of electric fields near the metal surface. The strength of the SPPs' electric field decays exponentially into the dielectric side and the metal itself, with different decay length as shown in Fig. 2(b). It is clear that the SPPs belong to the class of evanescent fields. Its penetration depth into the dielectric side ($\delta_\mathrm{d}$) and the metal side ($\delta_\mathrm{m}$) are given by [37]

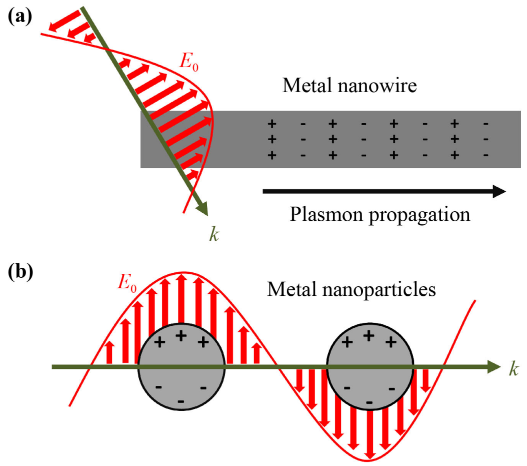

**Fig. 1** Schematic of **(a)** SPPs and **(b)** LSPRs. (a) The silver nanowire's length is larger than the wavelength of incident light and width is near the wavelength. (b) Silver nanospheres' size is much smaller than the wavelength of incident light (red).

$$\delta_\mathrm{d} = \frac{\lambda_\mathrm{spp}}{2n}, \tag{1.1a}$$

$$\delta_\mathrm{m} = \frac{\lambda_\mathrm{spp}}{2\pi}. \tag{1.1b}$$

Here, $\lambda_\mathrm{spp}$ is the plasmon frequency and $n$ is the refractive index of the dielectric side. It can be easily found from Eq. (1.1) that the $\delta_\mathrm{m}$ is normally smaller than $\delta_\mathrm{d}$ due to a smaller value of $n$ than $\pi$ in the denominator.

### 1.1.2 Plasmon frequency

The wavevector of the SPPs is given by $k_\mathrm{spp} = n_\mathrm{spp}k_0$ where $k_0 = \frac{\omega}{c}$ is the original wavevector of the light field and $n_\mathrm{spp}$ is the refractive index of the SPPs:

$$n_\mathrm{spp} = \frac{c}{v_\mathrm{spp}}. \tag{1.2}$$

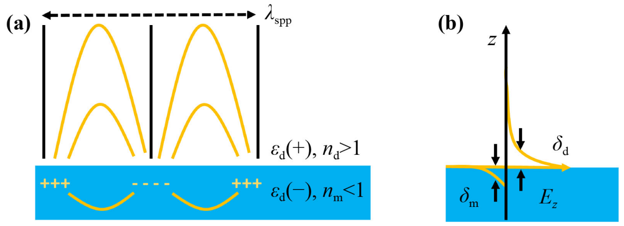

**Fig. 2** Schematic diagram of **(a)** charge distribution of the SPPs modes on the interface (black solid curves represent strength of electrical field) and **(b)** decay of electrical field through interface between metal and dielectric.

In Eq. (1.2), $v_{\text{spp}}$ is the phase velocity of SPPs and $c$ is the speed of light in vacuum,

$$v_{\text{spp}} = \frac{c}{\sqrt{\epsilon_{\text{spp}}}}. \tag{1.3}$$

Here, $\epsilon_{\text{spp}} = \frac{\epsilon_{\text{d}}\epsilon_{\text{m}}}{\epsilon_{\text{d}}+\epsilon_{\text{m}}}$ is the effective relative permittivity experienced by the SPPs [38]. $\epsilon_{\text{d}}$ and $\epsilon_{\text{m}}$ are the relative permittivity of dielectric and metal beside the interface. Therefore, we can get Eq. (1.4) from above:

$$k_{\text{spp}} = \frac{\omega}{c}\sqrt{\frac{\epsilon_{\text{d}}\epsilon_{\text{m}}}{\epsilon_{\text{d}}+\epsilon_{\text{m}}}}. \tag{1.4}$$

### 1.1.3 Dispersion relation

In classical theory, the permittivity depends on the frequency of the light, which will lead to frequency-dependent propagation (dispersion) for SPPs. For simplicity here, the Lorentz–Drude (LD) model is used, which only considers free-electron (intraband) effects rather than bound-electron (interband) effects [39]. Using this model, the complex permittivity of the metal can be written as a function of the form [40]:

$$\epsilon = \epsilon_x + \mathrm{i}\epsilon_y = 1 - \frac{\omega_{\text{p}}^2}{\omega^2 + \mathrm{i}F\omega}. \tag{1.5}$$

Here, $\omega$ is the angular frequency of light field, $F$ is the damping frequency (rate) related with the mean path of electrons (inverse of lifetime of electrons' free movement) [40] and $\omega_{\text{p}}$ is the plasmon frequency depending on intraband transitions of electrons ($\omega_{\text{p}}^2 = \frac{Ne^2}{m\epsilon_0}$, where $N$ is concentration of free electrons in metal and $\epsilon_0$ is permittivity of vacuum). $F$ and $\omega_{\text{p}}$ are both characteristic parameters. We can easily find that a high damping rate ($F$) is disadvantageous for the enhancement of the electric field.

Provided the damping rate is neglected, Eq. (1.5) can become

$$\epsilon = 1 - \frac{\omega_{\text{p}}^2}{\omega^2}. \tag{1.6}$$

In addition, it should be noted that the quantum confinement will appear which is negative for the electric field enhancement of SPPs (coupling strength) if the light field is confined into the nanoscale [41]. However, this phenomenon has less influence on strong coupling since the mode volume of SPPs is enough spacious to avoid quantum confinement [1].

For SPPs propagating along the interface between metal and air, we still consider the permittivity of the metal based on the LD model as mentioned above. Therefore, we can derive the dispersion relation of $k_{\text{spp}}$ and $\omega$ from Eqs. (1.4) and (1.6) ($k_{\text{spp}} \equiv k$ due to):

$$\omega^2 = ck_{\text{spp}}^2 + \frac{1}{2}\omega_{\text{p}}^2 \pm \sqrt{ck_{\text{spp}}^4 + \frac{1}{4}\omega_{\text{p}}^4}. \tag{1.7}$$

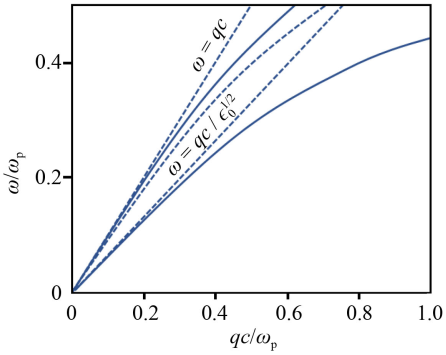

**Fig. 3** Dispersion curve (solid curves) of the SPPs. The horizontal coordinate is the in-plane wavevector (parallel to the interface) of light and the vertical coordinate is the angular frequency of the SPPs. Dashed straight lines present the relationship between angular frequency and in-plane wavevector of light in air and dielectric ($\epsilon_0$ is permittivity of the dielectric). The dashed curve represents the dispersion curve of the mental film without dielectric cladding.

We find that there are two branches in dispersion relation corresponding to "±" in Eq. (1.7). For light propagating in dielectric or air, it meets a relation:

$$\omega = ck = \frac{ck_0}{n} = \frac{ck_0}{\sqrt{\epsilon}}. \tag{1.8}$$

Here, $c$ is the light speed in vacuum, $\epsilon$ is the relative permittivity of the dielectric ($\epsilon = 1$ for air and vacuum) and $k_0$ is the wavevector of the light propagating in air.

Figure 3 shows the dispersion curve of SPPs based on Eqs. (1.4) and (1.6) [42]. It is obvious that the in-plane wavevector (momentum) of SPPs is always larger than that of the incident light for the same angular frequency, which is ascribed to the dieletric constant sum being lower than zero [43]. Only if the wavevector of the incident light $k$ is equal to $k_{\text{spp}}$, called the momentum (wavevector) matching condition, light can couple to SPPs [44]. Therefore, the incident light freely propagating in the dielectric is unable to excite SPPs on the planar metal surface. However, the excitation of SPPs can be realized by some special methods such as prism or diffraction coupling, and non-linear mixing, as depicted in the following sub-section.

**Prism coupling**

The wavevector of the incident light can be increased from $k_0$ to $nk_0$ when it enters into a prism of refractive index $n$ from air based on the relation: $n_1k_1 = n_2k_2$. Figure 4 shows two forms of prism coupling where $\theta_{\text{SP}}$ is the angle of light in the prism deviated from the normal of the prism's bottom interface. Therefore, the component parallel to the bottom interface of the wavevector can be obtained:

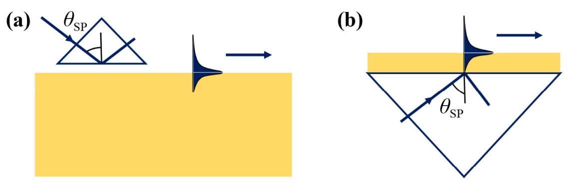

**Fig. 4** Schematic diagrams of prism coupling of incident light to SPPs with **(a)** Otto structure and **(b)** Kretschmann–Raether structure.

$$k = nk_0 \sin\theta_{\text{SP}}. \tag{1.9}$$

As is well known, there will be a total internal reflection when the incident angle of light is larger than the critical angle. Actually, when the total internal reflection occurs, there will be an evanescent field excited on the interface, decaying exponentially away from the interface. In addition, the incident field's in-plane wavevector can be made to be equal to $k_{\text{spp}}$. Hence, we can adjust the incident angle to make this evanescent field satisfy the matching conditions of momentum (wavevector) to couple to the SPPs.

Generally, there are two main structures of prism coupling. One is the Otto structure [Fig. 4(a)] where there is a narrow dielectric gap between the metal film and the prism [45]. The evanescent field of the prism can couple to the SPPs on the interface between air and the metal film. However, it is hard to accurately adjust the nanoscale thickness of the air gap. To overcome this barrier, the Kretschmann–Raether structure as shown in Fig. 4(b) was designed where a very narrow metal film is directly deposited on the bottom of the prism since the nanoscale thickness of metal thin films is relatively easier to control by deposition [46]. The evanescent field will couple to SPPs through the metal thin film.

**Diffraction coupling**

Alternatively, the surface of metal thin film can be engineered to be a periodical structure which can cause diffraction of light and make the in-plane wavevector ($k_x$) of the diffracted light the same as the wavevector ($k_{\text{spp}}$) of SPPs by adjusting the period of this grating, leading to coupling [42, 47, 48]. For example, Fig. 5 shows that diffraction of light occurs on the grating surface of the metal film. We can obtain 1D wavevector $k_{\text{out}}$ of in-plane scattered light based on Laue equations ($\Delta\boldsymbol{k} = \boldsymbol{k}_{\text{out}} - \boldsymbol{k}_{\text{in}} = \boldsymbol{G}$, here $\boldsymbol{G}$ is the reciprocal lattice vector) from [49, 50]:

$$k_{\text{out}}^2 = k_{\text{in}}^2 \sin^2\theta + m\left(\frac{2\pi}{a}\right)^2. \tag{1.10}$$

Here, $\theta$ is incident angle, $k_{\text{in}}$ is wavevector of incident light, $a$ is grating constant and $m$ is the diffraction order. Of course, there is another explanation that the SPPs rather than incident light are scattered [51]. In fact, the nature of these two explanation are same (they have fully same mathematical formulation and they can be thought as different forms of expression).

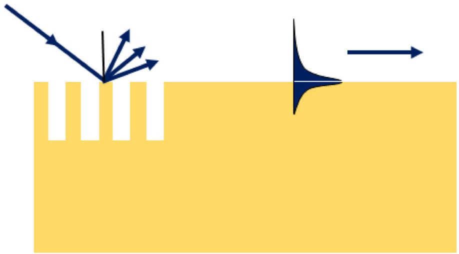

**Fig. 5** Schematic of diffraction coupling to SPPs by grating on surface of the metal film.

When coupling happens, a part of the incident optical energy hybridizes with the electronic oscillations resulting in a dip in the reflection spectrum (the dip centers in $k_{\text{in}}\sin\theta$ which meets momentum matching condition) as shown in Fig. 6 [52–54]. In Fig. 6, $L$ is the oscillation depth and $\theta_{\text{FWHM}}$ is the full width at half maximum of the dip which are proportional to coupling strength and loss of oscillation energy respectively ($Q$ value is inversely proportional to loss of oscillation energy) [55]. It should be noted that plasmonic cavities usually have a low $Q$ value, ascribed to their high loss. This high loss is the inevitable effect of the use of metals with negative real permittivity and a high concentration of free electrons [56].

When $k_{\text{out}}$ is identically equal to $k_{\text{spp}}$, we can get the relation between frequency $\omega$ and in-plane component of wavevector $k_x$ ($k_x = k_{\text{in}}\sin\theta$) from Eqs. (1.4) and (1.10) as shown in Fig. 7. It is salient that there exist band gaps avoiding occurrence of cross between SPPs of different diffraction orders.

### 1.1.4 Propagation length

The propagation distance of SPPs ($L_{\text{spp}}$) is defined to be the distance SPPs have travelled before decrease of the

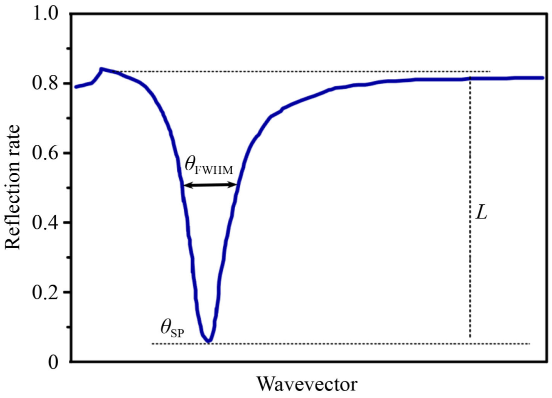

**Fig. 6** Reflection spectrum of metallic grating with a narrow dip corresponding to the excitation of plasmonic modes through grating coupling.

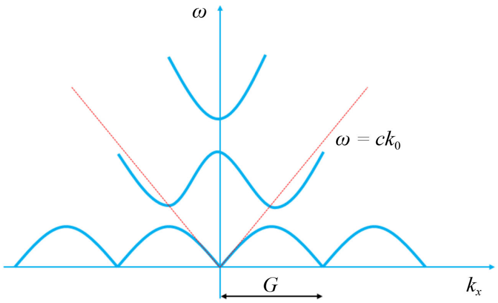

**Fig. 7** Dispersion of SPPs by diffraction coupling ($G=\frac{2\pi}{a}$).

intensity to 1/e of the initial value [37], depending on the imaginary part of the SPPs' wavevector [57]:

$$L_{\text{spp}}=\frac{1}{2\text{Im}\left(k_{\text{spp}}\right)}. \tag{1.11}$$

Because the metal has a complex relative permittivity:

$$\epsilon_{\text{m}}=\epsilon_{\text{m}}'+\text{i}\epsilon_{\text{m}}'' \tag{1.12}$$

and according to Eq. (1.4), the SPPs' wavevector $k_{\text{spp}}$ can be written as a complex form:

$$k_{\text{spp}}=k_{\text{spp}}'+\text{i}k_{\text{spp}}''=\frac{\omega}{c}\sqrt{\frac{\epsilon_{d(}\epsilon_{\text{m}}'+\text{i}\epsilon_{\text{m}}'')}{\epsilon_d+(\epsilon_{\text{m}}'+\text{i}\epsilon_{\text{m}}'')}}. \tag{1.13}$$

Assuming $\epsilon_{\text{m}}''<\epsilon_{\text{m}}'$, it can be obtained as [58]

$$k_{\text{spp}}'=\frac{\omega}{c}\sqrt{\frac{\epsilon_d\epsilon_{\text{m}}'}{\epsilon_d+\epsilon_{\text{m}}'}}, \tag{1.14a}$$

$$k_{\text{spp}}''=\frac{\omega}{c}\frac{\epsilon_{\text{m}}''}{2(\epsilon_{\text{m}}')^2}\left(\frac{\epsilon_d\epsilon_{\text{m}}'}{\epsilon_d+\epsilon_{\text{m}}'}\right)^{\frac{3}{2}}. \tag{1.14b}$$

Hence, the propagation distance $L_{\text{spp}}$ becomes

$$L_{\text{spp}}=\frac{c}{\omega}\frac{(\epsilon_{\text{m}}')^2}{\epsilon_{\text{m}}''}\left(\frac{\epsilon_d+\epsilon_{\text{m}}'}{\epsilon_d\epsilon_{\text{m}}'}\right)^{\frac{3}{2}}. \tag{1.15}$$

For metals with larger $\epsilon_{\text{m}}'$, a longer $L_{\text{spp}}$ can be obtained. Figure 8 shows the propagation length of SPPs along the surface of silver and air under visible and near infrared wavelength based on Eq. (1.15), in which the relative permittivity of silver is calculated by the Drude–Lorentz (LD) model with $\omega_{\text{p}}=1.2\times10^{16}$ rad·s$^{-1}$ and $F=1.45\times10^{13}$ s$^{-1}$ [59]. It can be found that the propagation length is much longer than the plasmon wavelength ($L_{\text{spp}}\gg\lambda_{\text{spp}}$), and across a wide spectral can be some hundreds of micrometers.

### 1.2 Localized Surface Plasmon Resonances (LSPRs)

Different from SPPs, LSPRs are confined in the adjacencies of metal nanoscale particles within subwavelength volume. When the incident light illuminates metal particles like nanospheres [Fig. 1(d)] with size much smaller than the wavelength of light, surface free electrons will be driven by the light's electric field to one end, resulting in only positive charges left in the other end [59]. In consequence, Coulomb interaction between opposite charges in two ends can provide a restoring force to sustain the oscillation [1]. Many structures such as metallic rods [60, 61], voids [62], discs [63] and cubes [64] can be used for the excitation of LSPRs.

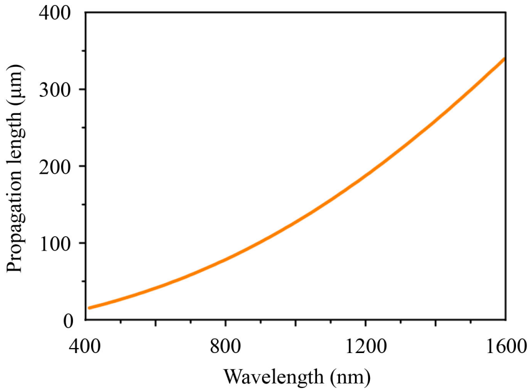

**Fig. 8** The propagation length of the SPPs as a function of the plasmon wavelength.

The resonance frequency of LSPRs is very sensitive to the geometry size and shape of the metal particles, and the surrounding dielectric material [42]. Comparing with the SPPs discussed above, LSPRs do not need to meet the momentum matching conditions of coupling since space translational invariance has been broken which means the momentum does not need to be conserved anymore [65]. Therefore, LSPRs can be directly excited by the incident light freely propagating in the dielectric.

## 2 Plasmonic hot electrons

SPs have two outcomes for the surface or near-surface free electrons that are excited on the metal: radiative decay to the emission of photons or non-radiative decay to the excitation of hot electrons. In the past, non-radiative decay was usually thought to be useless and disadvantageous until the discovery of hot-electron excitation. Hot electrons can be injected to the conduction bands of the semiconductor through the Schottky barrier, used for various applications [66]. In this section, the background knowledge of plasmonic hot electrons is systematically described with specific reference to generation principle, relaxation process, the injection probability and others.

### 2.1 Hot electron generation

#### 2.1.1 Photoexcitation hot electrons

Under the absolute zero temperature, electrons in metals obey the Fermi–Dirac distribution (orange solid line in

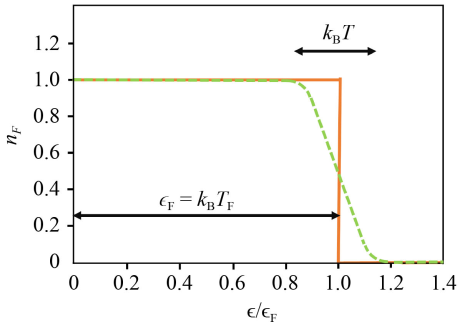

**Fig. 9** The Fermi–Dirac distribution at the absolute zero temperature (orange solid line), showing a step at the Fermi level. For $T > 0$, some electrons below $E_F$ can be thermally excited (green dotted curve).

Fig. 9) $f_e(E) = \frac{1}{1+\exp\left(\frac{E-E_F}{k_BT}\right)}$, showing the probability distribution of an electron of energy $E$ at temperature $T$ [67]. $f_e(E)$ is unity when $E < E_F$, while, $f_e(E) = 0$ for $E > E_F$. While $T > 0$, some electrons distributed in energy levels close to $E_F$ are likely excited to higher energy levels beyond $E_F$.

In 1887, Hertz [68] found earliest experimental phenomenon of photoelectric effect which was theoretically explained by Einstein [69] in 1905. According to Einstein's theory of the "Photoelectric Effect", light is composed of many independent photons whose energy $E$ is discrete equal to their frequency $\mu$ timing the Planck's constant $h$ $(E = h \times \mu)$. In brief, this theory illustrates that light can excite an electron from a metal substrate only if its frequency rather than intensity is beyond a threshold value decided by the metal substrate's work function.

When the energy of a photon is less than the work function of the metal, the electron will be excited to the higher energy level. This electron is defined as the photoexcitation hot electron. Carriers are classified as cold or hot carriers according to whether their energy are much larger than electrons from thermal excitation under ambient temperature [70].

When a photon with energy $\hbar\omega$ is absorbed by the metal, the distribution equilibrium of electrons under temperature $T$ is broken where one electron is excited with increase of energy by $\hbar\omega$ [red dashed in Fig. 10(a)] [71]. Then, this photoexcitation hot electron will experience fast electron–phonon [Fig. 10(b)] and electron–electron [Fig. 10(c)] collisions, resulting in transferring of energy from the hot electron to the lattice and other cold electrons close to the Fermi energy level.

### 2.1.2 Plasmonic hot electrons

As introduced above, surface plasmons (SPP and LSPR) are the collective oscillation of surface free electrons in metallic nanostructures caused by incident light which can effectively enhance local electric field. Then, surface plasmons will rapidly decay [72]. As shown in Fig. 11,

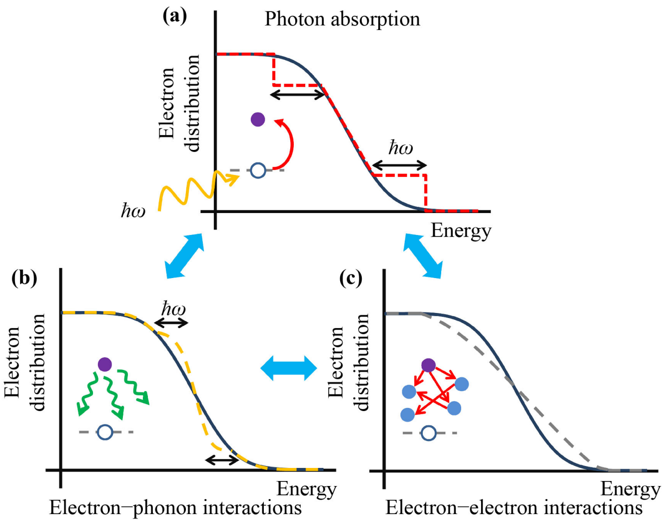

**Fig. 10** The electron distribution under **(a)** the absorption of a photon with energy $\hbar\omega$, **(b)** electron–phonon scattering and **(c)** electron–electron scattering.

their decay has two outcomes: one is rediative re-emission of a photon and the other is non-rediative damping to form electron–hole pairs within 100 fs, transferring their energy to electrons [73]. These electrons are called "hot electrons" and their energy is ranged from the Fermi level $E_F$ to $E_F + \hbar\omega_p$. Because plasmon energy $\hbar\omega_p$ is less than the plasmonic metal's work function, these hot electrons cannot escape to the vaccum [70]. Finally, these hot electrons will experience a very fast relaxation process in which their energy totally transformed into heat in the end [70, 72].

### 2.1.3 Difference between plamonic and photoexcitation hot-electron excitation

It is necessary to understand whether there is any difference between the hot electron generation from the absorption of a photon and a plasmon. Figure 12 shows energy compositions of one photon in the dieletric and one plasmon in the metal. The energy of one photon in the dieletric is mainly devided into the electric field energy $(\frac{1}{4}\varepsilon_0 E^2)$, magnetic field energy $(\frac{1}{4}\mu_0 H^2)$ and the potential energy of bound carriers. For one plasmon in the metal, the

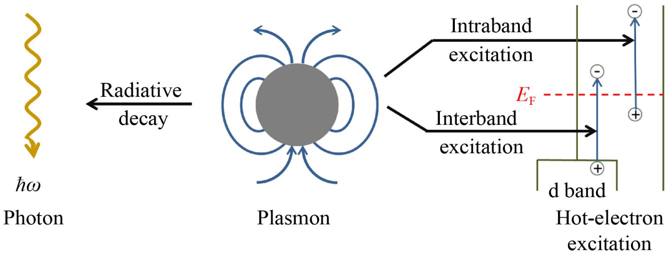

**Fig. 11** Schematic of radiative and non-radiative decay of plasmon.

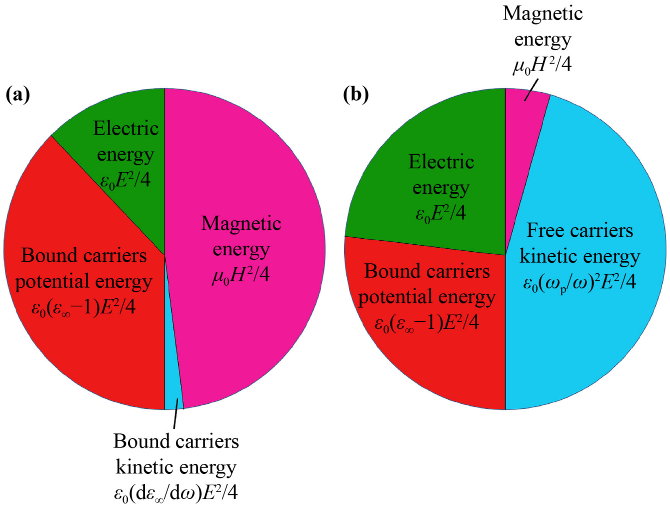

**Fig. 12** Energy composition distribution of **(a)** a photon polariton in dielectric and **(b)** a plasmon polariton in the metal.

energy is mainly composed of the electric field energy ($\frac{1}{4}\varepsilon_0E^2$), the potential energy of bound carriers and the kinetic energy of the collective motion of free carriers. Whereas, only the electric field can interact with one electron–hole pair in the metal or the dieletric according to the Hamiltonian $e\boldsymbol{r}\cdot\boldsymbol{E}$ [74]. Therefore, the physical nature of the absorption of a photon and a plasmon is identical.

## 2.2 Excitation mechanics of hot electrons

There are four main excitation chanels for plasmonic hot electrons as inroduced below [75]. As displayed in Fig. 13(a), for direct interband excitation in silver and gold, their band gap $E_{\mathrm{ds}}$ between Fermi level locating in s band and d shell is 3 eV and 2 eV respectively [76]. Therefore, only the ultraviolet excitation can overcome these barriers. For holes left in d shell, they can have a large potential energy relative to Fermi level due to their large effective mass. However, they have no access to reaching the metal surface because of their short mean free path ascribed to their small kinetic energy and ballistic velocity [75]. Only in the case that first-generation hole decays to three second-generation particles (two holes and one electron) in s band, it can become possible. Owing to decreased energy in this decay, the possibility for these second-generation particles is still rather low. Therefore, the direct interband transistion is unlikely for hot carriers injection.

The second path is phonon-assisted (or impurity-assisted) transitions, involving the absorption between two states of different wavevectors in the same s band, as shown in Fig. 13(b). Due to the mismatch of wavevector (momentum) between two states, a modification is required caused by a phonon or an impurity with wavevector $k$. Firstly, the plasmon is absorbed for the generation of a hot electron and a hot hole. The first-generation energy $E_{\mathrm{F}} < E < E_{\mathrm{F}} + \omega_{\mathrm{p}}\hbar$ for hot electrons and $E_{\mathrm{F}} > E > E_{\mathrm{F}} - \omega_{\mathrm{p}}\hbar$ for hot holes. Among it, all energy from plasmon is almost tranferred to the hot carriers without dissipation to carriers around the Fermi level.

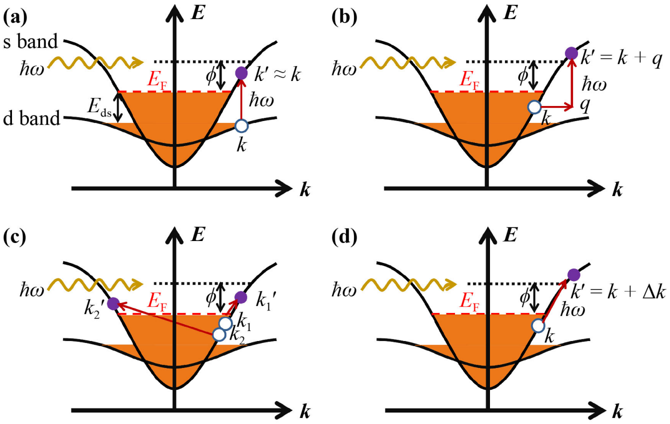

**Fig. 13** Four mechanics of non-radiative decay of plasmon: **(a)** direct interband transition; **(b)** phonon (or impurity)-assisted decay; **(c)** interelectronic (EE) scattering-assisted decay; **(d)** Landau damping or surface collision-assisted decay.

The third approach is electron–electron (EE) scattering-assisted transitions [Fig. 13(c)] where two hot electrons and two hot holes share the energy from the decay of plasmon, with each average energy equal to $\frac{\omega_{\mathrm{p}}\hbar}{4}$ [77]. At low frequencies, the EE scattering plays a negligible role in electrical resistance since the total momentum is conserved [75]. Hence, energy will be constant without any loss in EE scattering. However, for optical frequency, the energy of photon is high enough for the activation of the Umklapp processes where one electron can be excited to adjacent Brillouin zone so that momentum conservation becomes $k_1 + k_2 = k_1' + k_2' + g$ ($g$ is the reciprocal lattice vector) [78]. The EE scattering-assisted plasmon damping rate is defined by $\gamma_{ee} = F_{\mathrm{U}}\left(\omega\right) \times \tau_{\mathrm{ee}}^{-1}\left(\omega\right)$ where the EE scattering rate is $\tau_{\mathrm{ee}}^{-1} \approx \frac{\pi}{24}\frac{E_{\mathrm{F}}}{\hbar}\left(\frac{\hbar\omega}{E_{\mathrm{F}}}\right)^2$ regardless of temperature contributions and $F_{\mathrm{U}}\left(\omega\right)$ is the fraction of the Umklapp processes in the total EE scattering, usually the order of 0.2–0.5 [79]. As photon energy over 2 eV, this decay channel will dominate. But for the photon energy less than 1 eV, its effects can be neglected.

The forth decay channel is surface collision-assisted transitions in classic physics [80] or Landau damping in quantum picture [81] [Fig. 13(d)]. Classically, the collision of an electron with the surface can cause the energy transfer between the electron and the lattice like collision of an electron with a phonon or defect. During this process, surface collision rate [82] is $\gamma_{\mathrm{surf}} = A\frac{v_{\mathrm{F}}}{d}$ ($A$ is a dimensionless constant depending on the particular nanoparticle shape as well as material parameters of the metal and the surrounding dielectric matrix, $d$ is the size of the nanoparticle and $v_{\mathrm{F}}$ is the Fermi velocity about $1.4 \times 10^8$ cm/s for Au and Ag) [83]. Landau damping is not required to follow the momentum conservation rules since a recoil occurs in the collision with metal surface, resulting in the production of a phonon [84]. Hot electrons generated by surface collision (Landau damping) only exist within a thin layer of thickness $\Delta L = \frac{2\pi}{\Delta k} = \frac{v_{\mathrm{F}}}{\omega}$ [74]. For example of gold under 700 nm excitation, the thickness is only about 3 nm much shorter than the mean free path 10–20 nm of interelectonic collisions ($L_{\mathrm{mfp}} = v_{\mathrm{F}}\tau_{\mathrm{ee}}$). Therefore, half of the carriers excited by Landau damping can reach the metal surface, accounting for Landau damping as the dominated mechanic for hot-electron injection from the metal.

## 2.3 Relaxation process of hot electrons

The whole relaxion process with timescale after excitation of LSPRs is mainly devided into four steps exhibited in Fig. 14 [85]. Initially, at $t = 0$ s, the light illuminates on a metallic nanoparticle to excite LSPRs [Fig. 14(a)]. LSPRs can enhance local electric field contributing to light absorption of metal.

Subsequently, as shown in Fig. 14(b), the plasmon resonance will fully decay with rediation of photon or to an electron hole pair within the lifetime $\tau$ from 1 fs to 100 fs via non-radiative decay ($\tau_{\mathrm{p}} = \gamma^{-1}$). Suppressed radiative damping is beneficial for generation of hot electrons[86]. These hot electrons always get confined in the metallic nanostructure because work function of metal is much larger than LSPRs energy.

Then, after the electron–electron collision within timescale ranging from 100 fs to 1 ps, a thermal equilibrium among hot electrons [Fig. 14(c)] will be realized between electrons in this stage with the electron temperature $T_{\mathrm{e}}$ obviously higher than lattice temperature $T_{\mathrm{L}}$ [87]. This process redistributes initial hot electrons' energy to other lower-energy electrons via the scattering and forms the Fermi–Dirac statistics under electron temperature $T_{\mathrm{e}}$. It should be noted that scattering between electrons may occur many times since only a small fraction of energy is transferred each time. Moreover, the once time of the electron phonon scattering $\tau_{\mathrm{ep}}$ roughly has the same order of magnitude as $\tau_{\mathrm{ee}}$ (the once time of inter-electronic scattering), and electron–phonon collisions in this period can be neglected due to its low energy loss [75].

Afterwards, it will take 5–10 picoseconds $\tau_{\mathrm{el}}$ to reach equilibration with lattice because electron phonon scattering need to happen many times [87]. It is noteworthy that $\tau_{\mathrm{el}}$ is totally different from $\tau_{\mathrm{ep}}$. Finally, as shown in Fig. 14(d), the lattice and hot electrons will cool down when all energy is transferred to the surrounding on a timescale from 100 ps to 10 ns depending on the metal material, the particle size and the themal conduction property of the environment [70].

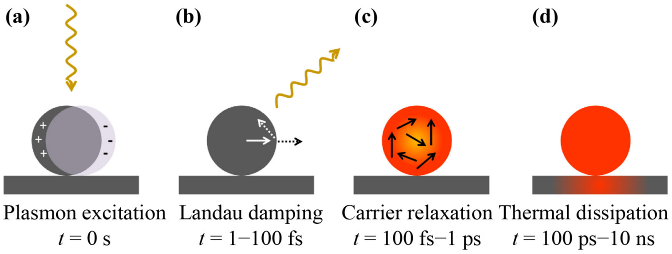

**Fig. 14** Schematic of relaxation process of plasmonic hot electrons inside metallic nanospheres.

## 2.4 Generation of equilibrium hot electrons

### 2.4.1 Redistribution of energy by electron–electron collisions

As the plasmon decays ($E = \hbar\omega$) shown Fig. 15(a), it will take $\tau_{\mathrm{p}}$ to excite a single pair of hole and electron with energy $E_{1,n}$ ($n = 1$, 2) as the first-generation carriers [Fig. 15(b)], with the energy sum of carriers $\sum_{n=1}^{2} E_{1,n} = \hbar\omega$. After the time $\tau_{\mathrm{ee}}$, around 10 fs [calculated from the equation $\tau_{\mathrm{ee}}^{-1} \approx \frac{\pi}{24}\frac{E_{\mathrm{F}}}{\hbar}\left(\frac{\hbar\omega}{E_{\mathrm{F}}}\right)^2$], either the elctron or the hole rapidly scatters with one electron below the Fermi level, forming another electron–hole pair. Hence, a total of three second-generation electron–hole pairs will appear when both the first-generation electron and hole scatter once. Each second-generation carrier has energy $E_{2,n}$ and $\sum_{n=1}^{6} E_{2,n} = \hbar\omega$. Likewise, each of the second-generation carriers can excite three third-generation carriers each with energy $E_{3,n}$ and $\sum_{n=1}^{18} E_{3,n} = \hbar\omega$. Without extraction, the whole process will continue until the average energy of the $X$-th generation carriers $\langle E_{X,n}\rangle_n = \hbar\omega/(2 \times 3^{X-1})$ is approaching $k_{\mathrm{B}}T_{\mathrm{L}}$ ($T_{\mathrm{L}}$ is the lattice temperature).

### 2.4.2 Temperature of equilibrium electrons

The energy density $u_{\mathrm{P}}$ of the surface plasmon per unit volume under unit time can be obtained from:

$$u_{\mathrm{P}} = F^2 I_{\mathrm{IN}}/v = F^2 I_{\mathrm{IN}} n/c, \tag{2.1}$$

where $I_{\mathrm{IN}}$ is the incident power density, $v$ is the phase velocity of light ($v = \frac{c}{n}$, $c$ is the speed of light and $n$ is the refract index), $F$ is the electric filed enhancement of the surface plasmon relative to the incident electric field. Assuming the energy is stored in the electron gas, the increase of the average temperature is defined as below [75]:

$$\overline{T}_{\mathrm{e}} - T_{\mathrm{L}} \sim \frac{\gamma_{\mathrm{nrad}}\tau_{\mathrm{el}}}{C_{\mathrm{el}}} u_{\mathrm{P}} = \frac{\gamma_{\mathrm{nrad}}\tau_{\mathrm{el}}}{C_{\mathrm{el}}} F^2 I_{\mathrm{IN}} n/c. \tag{2.2}$$

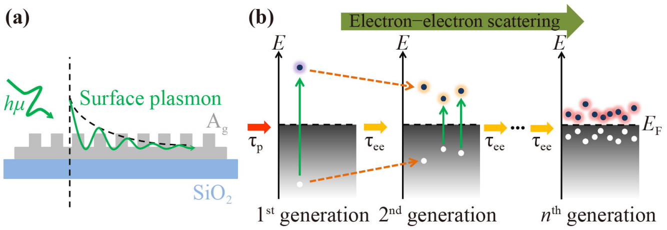

**Fig. 15** Schematic of generation of non-equilibrium hot carriers in the metal. **(a)** Illuminating a periodic metallic grating. **(b)** Step-wise excitation and decay of plasmon resonances to generate hot electrons.

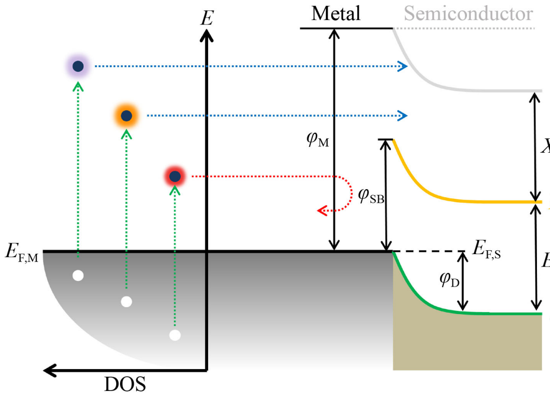

**Fig. 16** Left: Excitation of hot electrons in the metal from occupied energy levels (grey shade) resided below the Fermi level ($E_{F,M}$) to unoccupied levels beyond $E_{F,M}$. Right: The band diagram of the Schottky junction between the metal and the n-type semiconductor. Only hot electrons with energy over the schottky barrier $\varphi_{SB}$ can have access to injection to the semiconductor.

Here, $\gamma_{nrad}$ is the total non-radiative rate and $C_{el}$ is the heat capacity of electrons [88, 89]:

$$C_{el}=\frac{\pi^2}{2}\frac{k_B{}^2T}{E_F}N_e\approx 0.025k_BN_e\approx 0.018\ \mathrm{J/(K\cdot cm^3)},\tag{2.3}$$

where $E_F=5.56$ eV is Fermi energy of Au and $N_e\sim 60$ nm$^{-3}$ is the free electrons density of Au.

For metal nanospheres, $\gamma_{nrad}\sim\gamma_{LD}=0.75v_Fd$ ($d$ is the size and $v_F$ is the Fermi velocity) [75]. For an example of 10 nm silver nanospheres with $\tau_{el}$ of 10 ps, $\gamma_{nrad}\tau_{el}$ can be calculated to be ~ $10^3$ s$^{-1}$. By subsitituting Eq. (2.3) into Eq. (2.2), we can obtain:

$$\overline{T}_e-T_L\sim 2\times10^{-6}F^2I_{IN}.\tag{2.4}$$

Even if $F^2=10^3$ and $I_{IN}=100$ W/cm$^2$ (comparable to 1000 sun), the rise of the average electron temperature is only 0.2 K. Of course, the temperature of initial hot electrons should be much higher.

## 2.5 Injection of hot electrons to semiconductors

Figure 16 displays a diagram of the Schottky conjunction at the interface of the metal and an n-type semiconductor. With energy $E_e$ more than Schottky barrier $\varphi_{SB}$ ($E_e>\varphi_{SB}$), hot electrons can overcome the barrier and tranfer to unoccupied conduction band energy levels of the semiconductor [90]. When $E_e<\varphi_{SB}$, they will rebound. For p-type semiconductors, holes in place of electrons will be emitted from metallic nanostructures. However, the requirement of energy over $\varphi_{SB}$ as an essential basis does not mean the certain injection of hot electrons to semiconductors, but it also depends on the transport efficiency and the extraction efficiency.

### 2.5.1 Probability of hot-electron generation

The probability of one electron at the depth $z$ from the interface which are excited to energy $E$ above the Fermi level by one photon can be defined as [91]

$$P_{ex}(E,z)=P_e(E)\cdot\eta_{abs}(z),\tag{2.5}$$

where $P_e(E)$ is the normalized distribution function for electrons excited to energy $E$ and $\eta_{abs}(z)$ represents the ratio of the number of photons absorbed per unit volume at the depth $z$ to the number of photons incident per unit area of the irradiated interface.

As mentioned above, there is no apparent distinction between hot electrons excited by the SP and one photon. Therefore, Eq. (2.5) is fully applicable for the plasmonic hot-electron excitation. We built a calculation model for the number of hot electrons injecting to the semiconductor where the SP ($E_P$) is absorbed by the metal within the corresponding penetration depth $z$ to excite hot electrons beyond the $\varphi_{SB}$ [37]. Among this model, $P_{ex}(E,z)$ represents the probability that one electron at the depth $z$ from the interface is excited to energy $E$ above the Fermi level by the single SP ($E_P$).

Irrespective of the thermal kinetic energy ($T=0$), $P_e(E)$ can be obtained by [92]

$$P_e(E)=\begin{cases}\dfrac{3}{2E_F^{\frac{3}{2}}}(E+E_F-E_P)^{\frac{1}{2}}, & 0\le E\le E_P,\\ 0, & \text{Other},\end{cases}\tag{2.6}$$

where $E_F$ is the Fermi level of the metal. Considering the interface consisting of a thick dieletric and a thick metal, the p-polarized $\eta_{abs,\,P}(z)$ is given by [93]

$$\eta_{abs,\,P}(z)=(1-|r_p|^2)\cdot\alpha_p\cdot\exp(-\alpha_p\cdot z).\tag{2.7}$$

In Eq. (2.7), $r_p$ is the p-polarised amplitude reflectance of the SP which should be zero due to full non-radiative decay of the SP to hot-electron excitation and $\alpha_p$ is the p-polarised absorption coefficient of the metal, depending on the imaginary part of $\xi_p$:

$$\alpha_{\mathrm{p}} = 2\mathrm{Im}\left(\xi_{\mathrm{p}}\right), \tag{2.8}$$

where $\xi_{\mathrm{p}}$ is the wavevector propagating in the metal:

$$\xi_{\mathrm{p}} = \frac{2\pi}{\lambda_{\mathrm{P}}}\sqrt{\varepsilon_{\mathrm{m}}}. \tag{2.9}$$

Here, $\varepsilon_{\mathrm{m}}$ is the relative permittivity of the metal and $\lambda_{\mathrm{P}}$ is the SP wavelength. According to Eqs. (2.7)–(2.9), $\eta_{\mathrm{abs,\,P}}(z)$ becomes

$$\eta_{\mathrm{abs,\,P}}(z) = \frac{4\pi}{\lambda_{\mathrm{P}}}\mathrm{Im}\left(\sqrt{\varepsilon_{\mathrm{m}}}\right)\cdot\exp(-2\mathrm{Im}\left(\frac{2\pi}{\lambda_{\mathrm{P}}}\sqrt{\varepsilon_{\mathrm{m}}}\right)\cdot z). \tag{2.10}$$

For the pump fluence $F_{\mathrm{pump}}$, the density of the SP $(n)$ on the metal resonator can be gained by

$$n = \frac{F_{\mathrm{pump}}}{e}\cdot A\cdot\mathit{\Gamma}, \tag{2.11}$$

where $e$ is the electron charge, $A$ is the optical absorbance of the plasmonic resonator and $\mathit{\Gamma}$ is the enhancement of the electric-field intensity $\left(\left|\frac{E}{E_0}\right|^2\right)$.

Consequently, under the pump fluence $F_{\mathrm{pump}}$, the probability $(P_{\mathrm{pump}})$ of one electron at the depth $z$ from the interface excited to energy $E\,(0 \le E \le E_{\mathrm{P}})$ above the Fermi level can be obtained by the combination of Eqs. (2.5), (2.6), (2.10) and (2.11):

$$\begin{aligned} P_{\mathrm{pump}}(E,z) =& n\cdot P_{\mathrm{ex}}(E,z) \\ =& 6\pi\frac{F_{\mathrm{pump}}}{\lambda_{\mathrm{P}}e}\cdot A\cdot\mathit{\Gamma}\cdot\frac{(E+E_{\mathrm{F}}+E_{\mathrm{P}})^{\frac{1}{2}}}{E_{\mathrm{F}}^{\frac{3}{2}}} \\ &\cdot\mathrm{Im}\left(\sqrt{\varepsilon_{\mathrm{m}}}\right)\cdot\exp\left(-2\mathrm{Im}\left(\frac{2\pi}{\lambda_{\mathrm{P}}}\sqrt{\varepsilon_{\mathrm{m}}}\right)\cdot z\right). \end{aligned} \tag{2.12}$$

### 2.5.2 Transport efficiency

The injection efficiency of hot elections into semiconductors is divided into two factors: the transport efficiency $\eta_{\mathrm{trans}}$ and the extraction efficiency $\eta_{\mathrm{ext}}$ [75]. $\eta_{\mathrm{trans}}$ is defined as $\eta_{\mathrm{trans}} = \frac{N_{\mathrm{s}}}{N_0}$ where $N_{\mathrm{s}}$ is the number of hot electrons reaching the surface of the metal and $N_0$ is the number of hot electrons excited in the metal. We assume that the initial movement direction of all hot electrons is perpendicular to the interface. Therefore, $\eta_{\mathrm{trans}}$ at the depth $z$ can be obtained by [92]

$$\eta_{\mathrm{trans}}(E,z) = \frac{1}{2}\exp\left(-\frac{z}{L_{\mathrm{mfp,e}}(E)}\right), \tag{2.13}$$

where $L_{\mathrm{mfp,e}}(E)$ is the inelastic mean free path of the electrons in the metal and the coefficient $\frac{1}{2}$ means that half of hot electrons move opposite to the interface. $L_{\mathrm{mfp,e}}(E)$ is defined as [94]

$$L_{\mathrm{mfp,e}}(E) \sim 4(1+R_{\mathrm{s}})\frac{(E+E_{\mathrm{F}})E_{\mathrm{F}}}{E^2}. \tag{2.14}$$

Here, $R_{\mathrm{s}} = 3.02\,\mathrm{a.u.}$ for silver and gold.

### 2.5.3 Extraction efficiency

The extraction efficiency $\eta_{\mathrm{ext}}$ represents the probability of hot electrons across the Schottky barrier $\varphi_{\mathrm{SB}}$ ($\eta_{\mathrm{ext}} = \frac{N_{\mathrm{inj}}}{N_{\mathrm{s}}}$ where $N_{\mathrm{inj}}$ is the number of hot electrons injecting to the semiconductor). For a hot electron with energy $E$ beyond the Fermi level in the metal, its wavevector $k_{\mathrm{m}}$ can be gained by

$$k_{\mathrm{m}} = \frac{\sqrt{2m_{\mathrm{m}}E}}{\hbar}. \tag{2.15}$$

$m_{\mathrm{m}}$ is the effective mass of electrons in the metal. Through the Schottky barrier $\varphi_{\mathrm{SB}}$, the wavevector $k_{\mathrm{s}}$ in the semiconductor becomes

$$k_{\mathrm{s}} = \frac{\sqrt{2m_{\mathrm{s}}(E-\varphi_{\mathrm{SB}})}}{\hbar}. \tag{2.16}$$

Here, $m_{\mathrm{s}}$ is the effective mass of the electron in the semiconductor. The direction perpendicular to the interface is defined as the $x$ axis as shown in Fig. 17. For hot electrons with angle $\theta_{\mathrm{m}}$ in the metal therefore, their $x$-components are as below:

$$k_{\mathrm{m,x}} = k_{\mathrm{m}}\cdot\cos\theta_{\mathrm{m}}, \tag{2.17}$$

$$k_{\mathrm{s,x}} = k_{\mathrm{s}}\cdot\cos\theta_{\mathrm{s}}. \tag{2.18}$$

Here, $\theta_{\mathrm{m}}$ and $\theta_{\mathrm{s}}$ are angles of the normal of the interface with the wavevector direction of the hot electron in the metal and the semiconductor respectively. To overcome the Schottky barrier, the $x$-component in the metal should satisfy

$$k_{\mathrm{m},x} > \frac{\sqrt{2m_{\mathrm{m}}\varphi_{\mathrm{SB}}}}{\hbar}. \tag{2.19}$$

According to Eqs. (2.15), (2.17) and (2.19), we can know:

$$\theta_{\mathrm{m}} < \arccos\sqrt{\frac{\varphi_{\mathrm{SB}}}{E}}. \tag{2.20}$$

For the smooth interface, the lateral (in plane) wavevector across the Schottky barrier is continuous,

$$k_{\mathrm{m},//} = k_{\mathrm{m}}\cdot\sin\theta_{\mathrm{m}} = k_{\mathrm{s}}\cdot\sin\theta_{\mathrm{s}} = k_{\mathrm{s},//}. \tag{2.21}$$

As $\theta_{\mathrm{s}} = 90°$, $\theta_{\mathrm{m}}$ also needs to be smaller than the critical angle, we can get the other relation:

$$\theta_{\mathrm{m}} < \arcsin\sqrt{\frac{(E-\varphi_{\mathrm{SB}})m_{\mathrm{s}}}{E\cdot m_{\mathrm{m}}}}. \tag{2.22}$$

Therefore, the extraction efficiency $\eta_{\mathrm{ext}}$ can be obtained

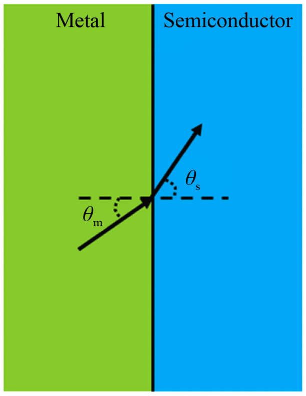

**Fig. 17** Schematic of hot-electron injection from metal to semiconductor across the interface.

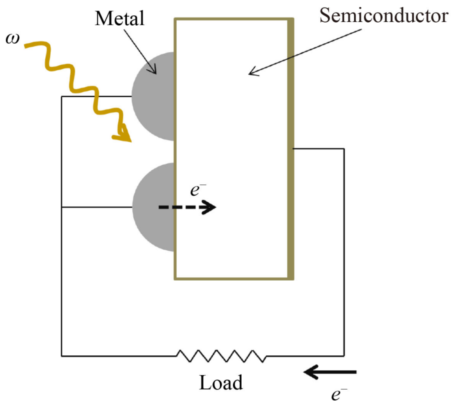

**Fig. 18** Diagram of photovoltaic cells based on current of hot electrons.

by the ratio of solid angles in spherical coordinates [95]:

$$\eta_{\text{ext}}(E)=\frac{\int_0^{2\pi}\int_0^{\Omega}\sin\theta\,\mathrm{d}\theta\,\mathrm{d}\varphi}{4\pi}=\frac{1}{2}(1-\cos\Omega), \tag{2.23}$$

where $\Omega$ is the smallest angle calculated from Eqs. (2.20) and (2.22). If $m_{\text{s}}=m_{\text{m}}$, the angle of Eq. (2.20) and Eq. (2.22) should be same since their quadratic sum is 1. Usually $m_{\text{s}}<m_{\text{m}}$, the result of Eq. (2.22) is always smaller than that of Eq. (2.20) for the same $E$.

For the non-smooth interface, the extraction efficiency only depends on the interface backscattering independent of injection angles of hot electrons, decided by densities of states in the metal and semiconductor [75].

As a consequence, the density $n_{\text{e}}$ of hot electrons injecting to QDs under the pump fluence $F_{\text{pump}}$ can be estimated by

$$n_{\text{e}}=\iint P_{\text{pump}}(E,z)\cdot\eta_{\text{trans}}(E,z)\cdot\eta_{\text{ext}}(E)\,\mathrm{d}E\mathrm{d}z. \tag{2.24}$$

Here, the integration range of energy $E$ should be $0$–$E_{\text{P}}$ and the depth $z$ should be from 0 to the penetration depth $\delta_{\text{m}}$ [37]:

$$\delta_{\text{m}}=\frac{1}{k}\left|\frac{\mathrm{Re}\,(\varepsilon_{\text{m}})+\varepsilon_{\text{s}}}{\mathrm{Re}\,(\varepsilon_{\text{m}})^2}\right|^{\frac{1}{2}}. \tag{2.25}$$

## 2.6 Applications of plasmonic hot electron

Plasmonic hot-electron injection has a broad application prospect. Subsequently, its important applications in photovoltaics and photodetection are described.

### 2.6.1 Photovoltaic cells

Photovoltaic cells can be composed of the circuit of metal and semiconductor as shown in Fig. 18. Under illumination, plasmonic hot electrons or holes in metal are continusly extracted across the Schottky junction to the semiconductor. Meanwhile, plasmonic metallic structures can be beneficial for light absorption due to scattering and trapping [96, 97]. It should be noted that the LSPRs of both silver and gold nanoparticles is in visible and infra-red spectral so that they are widely used in photovoltaic cells [98]. Generally, photocurrent generation based on hot electrons is successively divided into four key steps. Firstly, the metallic nanosturcture absorbs photons and hot electrons or holes are excited. Secondly, these hot electrons or holes in metal transport to the interface. Thirdly, hot electrons or holes pass the Schottky junction. Forthly, the semiconductor collects hot electrons or holes. It can be assumed that all hot electons or holes in interface are able to reach the semiconductor across the Schottky junction since these emitted carriers are also majority carriers in semiconductors leading in less recombination. Therefore, the forth step does not influence the photocurrent significanty. The approximation formula of current density response is [85]

$$\dot{J}=\dot{J}_{\text{sc}}-A^{*}T^{2}\mathrm{e}^{-\frac{\varphi_{\text{SB}}}{kT}}\left(\mathrm{e}^{\frac{V}{kT}}-1\right). \tag{2.26}$$

Here, $\dot{J}_{\text{sc}}$ is the short circuit photocurrent density, $V$ is the voltage over the cell and the right term is the reverse current density resulted by thermionic emission in Schottky junction introduced above. $\dot{J}_{\text{sc}}$ can be expressed as

$$\dot{J}_{\text{sc}}=q\int\varphi(\lambda)\,\eta_{\text{abs}}\eta_i(\lambda)\,\mathrm{d}\lambda. \tag{2.27}$$

Among this equation, $q$ is electron charge, $\varphi(\lambda)$ is the incident photon flux, $\eta_{\text{abs}}$ is the light absorption rate of the metal and $\eta_i$ is the electron emission efficiency including both passing via the metal and transfering over the Schottky junction. When a photon illuminates the metal surface without plasmonics, electrons will absorb it and be directly excited to an allowed state in the conduction band. However, for a flat metallic surface, the incident light will be mostly reflected causing low light absorption. If the metal surface is processed into the appropriate structure to excite SPs, light absorption can be significantly enhanced. Meanwhile, the plasmon

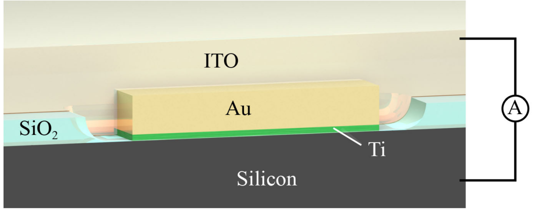

**Fig. 19** Diagram of a photodetector based on photocurrent of hot electrons.

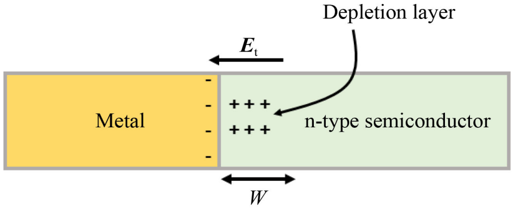

**Fig. 20** Charge distribution at the metal/n-semiconductor contact at the completion of the depletion layer.

will experience fast rediative dacay to emit a photon or nonrediative dacay to generate an electron–hole pair resulting in hot electrons.

### 2.6.2 Photodetection

Plasmonic resonators can absorb light to excite hot electrons, which can result in a photocurrent. In contrast to traditional photodetectors, plasmonic photodetectors can produce a detectable photocurrent when photon energies are above the Schottky barrier height but below the band gap of the semiconductor [99]. Hence, an appropriate selection of the semiconductor and the metal can realize the detection range beyond that determined solely by the band gap of the semiconductor. Figure 19 shows a type of plasmonic photodetector based on rectangular gold nanorods developed by Knight *et al.* [100], which has a Schottky conjunction formed on the interface of the Ti adhesion layer and the Si substrate with a barrier of 0.5 eV. An electrical circuit is built via the connection between the indium tin oxide (ITO) electrode and the silicon, where the insulator SiO$_2$ film blocks their contacts. Ultimately, experiments prove that a limiting wavelength of 2.5 μm can be detected.

## 3 Schottky conjunction

To harvest plasmonic hot electrons from the metal surface once SPPs or LSPRs have been excited, a Schottky conjunction formed on the contact of the metal with an adjacent semiconductor is required. In this section, the physics of Schottky conjunctions is introduced such as the formation mechanics, the barrier height and the current–voltage relationship.

### 3.1 Schottky barrier

When a metal contacts an n-type semiconductor with the Femi level higher than that of metal, electrons in the n-type semiconductor will transfer to the metal until the Femi level of both sides aligns at equilibrium [101]. As shown in Fig. 20, with increasing number of electrons entering the metal side, positive charges will gradually dominate in an interface area of the semiconductor's side called the depletion layer [101]. When the depletion layer is formed, there exists an electric field $\boldsymbol{E}_t$ produced by the opposite charges on two sides, leading in a potential barrier in the conjunction called "Schottky barrier" [101].

The work function $\phi_m$ of metals is equal to the energy difference between the Femi level to the vacuum level. It stands for the minimum kinetic energy for an electron to escape from the metal into air at $T = 0$ K [69]. In case of ideal metal/n-type semiconductor Schottky junction shown in Figs. 21(a, b), the barrier $\phi_{BN}$ is decided by the difference between work function $\phi_m$ of the metal and the electron affinity (valence band bottom) $\chi_s$ of the semiconductor [102]:

$$\phi_{BN} = \phi_m - \chi_s. \tag{3.1}$$

If $\phi_m$ is less than $\chi_s$ as shown in Figs. 21(c, d), the metal/semiconductor contact will become an ohmic contact and there will be no barrier for transit of carriers [103]. Similarly, the Schottky barrier $\phi_{BP}$ of the ideal Metal/p-type semiconductor Schottky contact can be written as [102]

$$\phi_{BP} = \frac{E_g}{q} - (\phi_m - \chi_s) = \frac{E_g}{q} - \phi_{BN}. \tag{3.2}$$

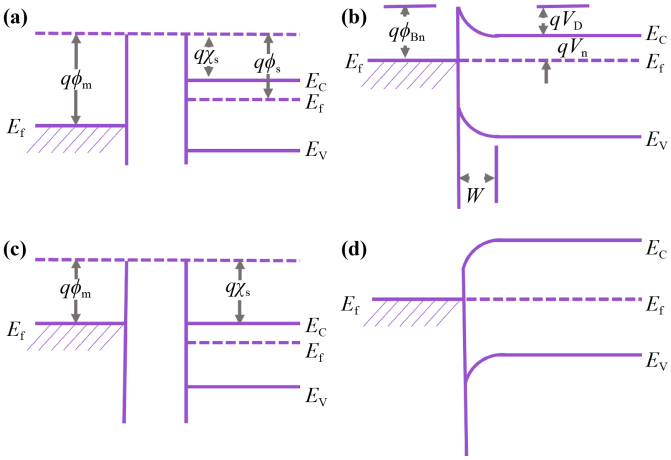

**Fig. 21** Energy band diagrams of a contact between the metal and the semiconductor: with $\phi_m > \chi_s$ **(a)** before contact and **(b)** in contact; with $\phi_m < \chi_s$ **(c)** before contact and **(d)** in contact.

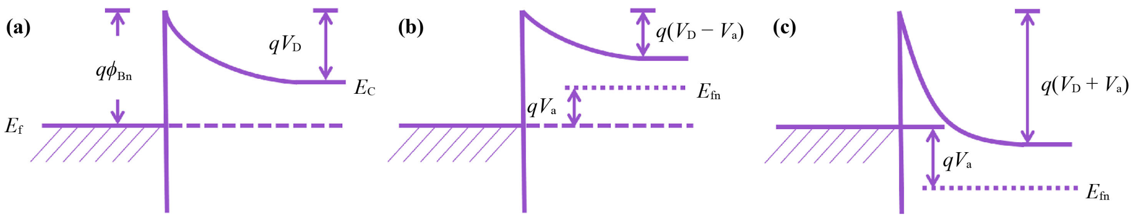

**Fig. 22** Illustration of energy band in Schottky junction under **(a)** no bias, **(b)** forward bias and **(c)** reserve bias $V_{\mathrm{a}}$.

Here, $E_{\mathrm{g}}$ is band gap and $q$ is electronic charge.

The contact potential $V_{\mathrm{D}}$ in a Schottky junction is defined as the differential of work function:

$$V_{\mathrm{D}}=\phi_{\mathrm{m}}-\phi_{\mathrm{s}}. \tag{3.3}$$

When a bias voltage $V_{\mathrm{a}}$ is provided to the Schottky junction, its energy band change is shown in Fig. 22 [102].

### 3.2 Current in Schottky conjunction

It should be noted that only the majority carrier of the semiconductor can contribute to the current flow in a Schottky conjunction, which is totally different from PN conjunctions whose minority carrier also drifts to the other side [104]. For a Schottky conjunction without bias, current from metal to n-type semiconductor $J_{\mathrm{ms}}$ is decided by barrier height $\phi_{\mathrm{BN}}$ and current from the opposite direction $J_{\mathrm{sm}}$ is controlled by contact potential $V_D$. For the case of forward bias, $J_{\mathrm{ms}}$ will not change because $\phi_{\mathrm{BN}}$ is constant, however, $J_{\mathrm{sm}}$ will obviously increase since the barrier in semiconductor side decreases to $V_{\mathrm{D}}-V_{\mathrm{a}}$. If under reverse bias, $J_{\mathrm{ms}}$ still keeps unchanged but $J_{\mathrm{sm}}$ will reduce due to increased barrier $V_{\mathrm{D}}+V_{\mathrm{a}}$.

Figure 23 reveals various transport approaches of carriers in Schottky conjunction under forward bias $V_{\mathrm{a}}$, including the thermionic emission (path a), the thermally enhanced field emission (path b), the multi-step tunneling (path c), the field emission (path d), the trapping states and subsequent emission (path e), the interface recombination (path f) and the drift of minority carriers (path g) [104].

Thermionic emission is a classical process without tunneling where majority carriers can inject to unoccupied levels in metal without any change of energy [102]. To pass the barrier, carriers' minimum kinetic energy must be equal or larger than it. The formula of its net current density $J_{\mathrm{OB}}$ for electrons over the barrier is defined as

$$J_{\mathrm{OB}}=-A^{*}T^{2}\mathrm{e}^{-\frac{q\phi_{\mathrm{B}}}{k_{\mathrm{B}}T}}\left(\mathrm{e}^{\frac{q\mathrm{V_a}}{k_{\mathrm{B}}T}}-1\right). \tag{3.4}$$

Here, barrier' height is $\phi_{\mathrm{B}}$ and $A^{*}$ is the effective Richardson constant equal to $4\pi m_{\mathrm{n}}^{*}qk_{\mathrm{B}}^{2}/h^{3}$, $m_{\mathrm{n}}^{*}$ is electrons' effective mass and $T$ is temperature. The minus symbol before $A^{*}$ is chosen since the current flowing to left is regarded as positive direction. It is also convenient to define:

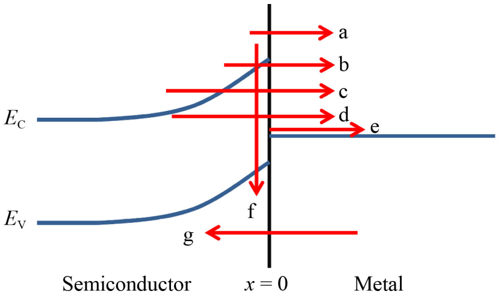

**Fig. 23** Illumination of interface transport mechanism in forward-biased Schottky conjunction (n-type semiconductor).

$$J_{0}=-A^{*}T^{2}\mathrm{e}^{-\frac{q\phi_{\mathrm{B}}}{k_{\mathrm{B}}T}}, \tag{3.5}$$

where $J_0$ is saturation current density from metal to semiconductor.

Thermally enhanced field emission is a direct tunneling process where electrons transfer from allowed states in semiconductors to allowed states in metal. It is slightly different from the field emission (path d) which is a tunneling process without thermal assist. Generally, this path may be dominant only under high-doping or high-temperature conditions.

Multistep tunneling is an indirect tunneling process from one defect to another defect in the barrier region which can interacts with phonons happening in doping levels and barrier thickness. Field emission is a direct tunneling where majority carriers in bottom of band cross the barrier in the semiconductor side. In this process, electrons in the conduction band located in interface ($x=0$) are initially trapped in a local state in or near interface and then emit to the metal. Its probability is decided by the population of majority carriers in all states involved during this process. When electrons are trapped in local states in interface, the interface recombination can occur. Since electrons as majority carriers transfer to the metal sides, holes as minority carriers will also be generated in valance band in metal side. These minority carriers in metal side can move to the semiconductor side by diffusion and drift.

## 4 Conclusion

In conclusion, we reviewed the latest description for the excitation of surface plasmons (SPs) and plasmonic hot electrons. Briefly, free electrons distributed on the metal surface are driven to collective oscillation by the incident light, leading to an electromagnetic wave in the subwavelength called the SP. In terms of the propagating property, SPs are divided into two types: Surface Plasmon Polaritons (SPPs) and Localized Surface Plasmon Resonances (LSPRs). Different from SPPs, the momentum conservation rule is not required for LSPRs due to the broken symmetric structure. Firstly, the SP non-radiatively decays to one plasmonic hot electron. It should be noted that there is no distinction between plasmonic hot electrons and hot electrons excited by the absorption of photons. Then, the plasmonic hot electron rapidly redistributes its energy to other electrons via the multiple scattering between electrons. Finally, all energy is transferred to the lattice by the multiple electron-phonon scttering. However before dissipation to the heat, plasmonic hot electrons whose energy is beyond the Schottky barrier can inject to the conduction band of the semiconductor through the Schottky conjunction, contributing to the device photocurrent or producing the electron doping. Furthermore, we presented a calculation model of the density of plasmonic hot electrons excited under the pump fluence $F_{\text{pump}}$. Therefore, plasmonic resonators are expected to be integrated in a wide range of optoelectronic devices, such as photovoltaic cells, to effectively improve their performance.

**Declarations** The authors declare that they have no competing interests and there are no conflicts.

**Acknowledgements** The work was supported by the Smart Ideas Fund by Ministry of Business, Innovation and Employment, New Zealand through contract UOOX1802 and the University of Otago, by means of the University of Otago Postgraduate Publishing Bursary (Doctoral).

## References

1. P. Törmä and W. L. Barnes, Strong coupling between surface plasmon polaritons and emitters: A review, *Rep. Prog. Phys.* 78(1), 013901 (2015)
2. Z. K. Zhou, J. Liu, Y. Bao, L. Wu, C. E. Png, X. H. Wang, and C. W. Qiu, Quantum plasmonics get applied, *Prog. Quantum Electron.* 65, 1 (2019)
3. J. A. Schuller, E. S. Barnard, W. Cai, Y. C. Jun, J. S. White, and M. L. Brongersma, Plasmonics for extreme light concentration and manipulation, *Nat. Mater.* 9(3), 193 (2010)
4. P. R. West, S. Ishii, G. V. Naik, N. K. Emani, V. M. Shalaev, and A. Boltasseva, Searching for better plasmonic materials, *Laser Photonics Rev.* 4(6), 795 (2010)
5. M. Rycenga, C. M. Cobley, J. Zeng, W. Li, C. H. Moran, Q. Zhang, D. Qin, and Y. Xia, Controlling the synthesis and assembly of silver nanostructures for plasmonic applications, *Chem. Rev.* 111(6), 3669 (2011)
6. T. Iqbal, M. U. Farooq, M. Ijaz, S. Afsheen, M. Rizwan, and M. B. Tahir, Optimization of 1D silver grating devices for extraordinary optical transmission, *Plasmonics* 14(5), 1099 (2019)
7. M. Zafar, M. Ijaz, and T. Iqbal, Efficient Au nanostructures for NIR-responsive controlled drug delivery systems, *Chem. Pap.* 75(6), 2277 (2021)
8. Y. He, K. Laugesen, D. Kamp, S. A. Sultan, L. B. Oddershede, and L. Jauffred, Effects and side effects of plasmonic photothermal therapy in brain tissue, *Cancer Nanotechnol.* 10(1), 8 (2019)
9. R. Lu, J. Ni, S. Yin, and Y. Ji, Responsive plasmonic nanomaterials for advanced cancer diagnostics, *Front. Chem.* 9, 652287 (2021)
10. R. G. Sobral-Filho, A. M. Brito-Silva, M. Isabelle, A. Jirasek, J. J. Lum, and A. G. Brolo, Plasmonic labeling of subcellular compartments in cancer cells: Multiplexing with fine-tuned gold and silver nanoshells, *Chem. Sci. (Camb.)* 8(4), 3038 (2017)
11. S. Ezendam, M. Herran, L. Nan, C. Gruber, Y. Kang, F. Gröbmeyer, R. Lin, J. Gargiulo, A. Sousa-Castillo, and E. Cortés, Hybrid plasmonic nanomaterials for hydrogen generation and carbon dioxide reduction, *ACS Energy Lett.* 7(2), 778 (2022)
12. Y. H. Jang, Y. J. Jang, S. Kim, L. N. Quan, K. Chung, and D. H. Kim, Plasmonic solar cells: From rational design to mechanism overview, *Chem. Rev.* 116(24), 14982 (2016)
13. M. Ijaz, A. Shoukat, A. Ayub, H. Tabassum, H. Naseer, R. Tanveer, A. Islam, and T. Iqbal, Perovskite solar cells: Importance, challenges, and plasmonic enhancement, *Int. J. Green Energy* 17(15), 1022 (2020)
14. T. Iqbal, M. Ijaz, M. Javaid, M. Rafique, K. N. Riaz, M. B. Tahir, G. Nabi, M. Abrar, and S. Afsheen, An optimal Au grating structure for light absorption in amorphous silicon thin film solar cell, *Plasmonics* 14(1), 147 (2019)
15. H. Zhang, F. Liu, R. J. Blaikie, B. Ding, and M. Qiu, Bifacial omnidirectional and band-tunable light absorption in free-standing core-shell resonators, *Appl. Phys. Lett.* 120(18), 181110 (2022)
16. Y. J. Lu, T. L. Shen, K. N. Peng, P. J. Cheng, S. W. Chang, M. Y. Lu, C. W. Chu, T. F. Guo, and H. A. Atwater, Upconversion plasmonic lasing from an organolead trihalide perovskite nanocrystal with low threshold, *ACS Photonics* 8(1), 335 (2021)
17. L. Gu, K. Wen, Q. Peng, W. Huang, and J. Wang, Surface-plasmon-enhanced perovskite light-emitting diodes, *Small* 16(30), 2001861 (2020)
18. J. A. Huang and L. B. Luo, Low-dimensional plasmonic photodetectors: Recent progress and future opportunities, *Adv. Opt. Mater.* 6(8), 1701282 (2018)
19. A. M. Shrivastav, U. Cvelbar, and I. Abdulhalim, A comprehensive review on plasmonic-based biosensors used in viral diagnostics, *Commun. Biol.* 4(1), 70 (2021)
20. J. Xavier, S. Vincent, F. Meder, and F. Vollmer, Advances in optoplasmonic sensors- combining optical nano/microcavities and photonic crystals with plasmonic nanostructures and nanoparticles, *Nanophotonics* 7(1),

1 (2018)

21. S. Afsheen, T. Iqbal, M. Aftab, A. Bashir, A. Tehseen, M. Y. Khan, and M. Ijaz, Modeling of 1D Au plasmonic grating as efficient gas sensor, *Mater. Res. Express* 6(12), 126203 (2019)
22. S. Afsheen, M. Munir, M. Isa Khan, T. Iqbal, M. Abrar, M. B. Tahir, J. U. Rehman, K. N. Riaz, M. Ijaz, and G. Nabi, Efficient biosensing through 1D silver nanostructured devices using plasmonic effect, *Nanotechnology* 29(38), 385501 (2018)
23. T. Iqbal, S. Noureen, S. Afsheen, M. Y. Khan, and M. Ijaz, Rectangular and sinusoidal Au-grating as plasmonic sensor: A comparative study, *Opt. Mater.* 99, 109530 (2020)
24. M. Ijaz, M. Aftab, S. Afsheen, and T. Iqbal, Novel Au nano-grating for detection of water in various electrolytes, *Appl. Nanosci.* 10(11), 4029 (2020)
25. S. Zhang, G. C. Li, Y. Chen, X. Zhu, S. D. Liu, D. Y. Lei, and H. Duan, Pronounced Fano resonance in single gold split nanodisks with 15 nm split gaps for intensive second harmonic generation, *ACS Nano* 10(12), 11105 (2016)
26. M. S. Verma and M. Chandra, Second harmonic generation-based nonlinear plasmonic RI-sensing in solution: The pivotal role of the particle size, *Phys. Chem. Chem. Phys.* 23(45), 25565 (2021)
27. A. Alù and N. Engheta, Plasmonic and metamaterial cloaking: Physical mechanisms and potentials, *J. Opt. A* 10(9), 093002 (2008)
28. H. Xu, Surface-enhanced Raman scattering beyond plasmonics, *Front. Phys.* 17(2), 23601 (2022)
29. L. Lan, Y. Gao, X. Fan, M. Li, Q. Hao, and T. Qiu, The origin of ultrasensitive SERS sensing beyond plasmonics, *Front. Phys.* 16(4), 43300 (2021)
30. L. Shi, B. Iwan, R. Nicolas, Q. Ripault, J. R. C. Andrade, S. Han, H. Kim, W. Boutu, D. Franz, T. Heidenblut, C. Reinhardt, B. Bastiaens, T. Nagy, I. Babushkin, U. Morgner, S. W. Kim, G. Steinmeyer, H. Merdji, and M. Kovacev, Self-optimization of plasmonic nanoantennas in strong femtosecond fields, *Optica* 4(9), 1038 (2017)
31. L. Shi, J. R. C. Andrade, A. Tajalli, J. Geng, J. Yi, T. Heidenblut, F. B. Segerink, I. Babushkin, M. Kholodtsova, H. Merdji, B. Bastiaens, U. Morgner, and M. Kovacev, Generating ultrabroadband deep-UV radiation and sub-10 nm gap by hybrid-morphology gold antennas, *Nano Lett.* 19(7), 4779 (2019)
32. L. Shi, J. R. C. Andrade, J. Yi, M. Marinskas, C. Reinhardt, E. Almeida, U. Morgner, and M. Kovacev, Nanoscale broadband deep-ultraviolet light source from plasmonic nanoholes, *ACS Photonics* 6(4), 858 (2019)
33. M. Hentschel, T. Utikal, H. Giessen, and M. Lippitz, Quantitative modeling of the third harmonic emission spectrum of plasmonic nanoantennas, *Nano Lett.* 12(7), 3778 (2012)
34. J. Geng, W. Yan, L. Shi, and M. Qiu, Surface plasmons interference nanogratings: Wafer-scale laser direct structuring in seconds, *Light Sci. Appl.* 11(1), 189 (2022)
35. L. Wang, Q. D. Chen, X. W. Cao, R. Buividas, X. Wang, S. Juodkazis, and H. B. Sun, Plasmonic nanoprinting: Large-area nanoscale energy deposition for efficient surface texturing, *Light Sci. Appl.* 6(12), e17112 (2017)
36. T. Zou, B. Zhao, W. Xin, Y. Wang, B. Wang, X. Zheng, H. Xie, Z. Zhang, J. Yang, and C. Guo, High-speed femtosecond laser plasmonic lithography and reduction of graphene oxide for anisotropic photoresponse, *Light Sci. Appl.* 9(1), 69 (2020)
37. W. L. Barnes, Surface plasmon-polariton length scales: A route to sub-wavelength optics, *J. Opt. A* 8(4), S87 (2006)
38. B. Ding, C. Hrelescu, N. Arnold, G. Isic, and T. A. Klar, Spectral and directional reshaping of fluorescence in large area self-assembled plasmonic-photonic crystals, *Nano Lett.* 13(2), 378 (2013)
39. A. D. Rakić, A. B. Djurišić, J. M. Elazar, and M. L. Majewski, Optical properties of metallic films for vertical-cavity optoelectronic devices, *Appl. Opt.* 37(22), 5271 (1998)
40. M. I. Markovic and A. D. Rakic, Determination of the reflection coefficients of laser light of wavelengths $\lambda \in$ (0.22 μm, 200 μm) from the surface of aluminum using the Lorentz–Drude model, *Appl. Opt.* 29(24), 3479 (1990)
41. J. A. Scholl, A. L. Koh, and J. A. Dionne, Quantum plasmon resonances of individual metallic nanoparticles, *Nature* 483(7390), 421 (2012)
42. A. V. Zayats, I. I. Smolyaninov, and A. A. Maradudin, Nano-optics of surface plasmon polaritons, *Phys. Rep.* 408(3–4), 131 (2005)
43. T. Iqbal and S. Afsheen, Coupling efficiency of surface plasmon polaritons for 1D plasmonic gratings: Role of under- and over-milling, *Plasmonics* 11(5), 1247 (2016)
44. S. Kasani, K. Curtin, and N. Wu, A review of 2D and 3D plasmonic nanostructure array patterns: Fabrication, light management and sensing applications, *Nanophotonics* 8(12), 2065 (2019)
45. A. Otto, Excitation of nonradiative surface plasma waves in silver by the method of frustrated total reflection, *Z. Phys.* 216(4), 398 (1968)
46. E. Kretschmann and H. Raether, Radiative decay of non-radiative surface plasmons excited by light, *Zeitschrift für Naturforschung A Phys. Sci.* 23, 2135 (1968)
47. T. Iqbal, Z. Ashfaq, S. Afsheen, M. Ijaz, M. Y. Khan, M. Rafique, and G. Nabi, Surface-enhanced Raman scattering (SERS) on 1D nano-gratings, *Plasmonics* 15(4), 1053 (2020)
48. S. Vempati, T. Iqbal, and S. Afsheen, Non-universal behavior of leaky surface waves in a one dimensional asymmetric plasmonic grating, *J. Appl. Phys.* 118(4), 043103 (2015)
49. G. Vecchi, V. Giannini, and J. Gómez Rivas, Shaping the fluorescent emission by lattice resonances in plasmonic crystals of nanoantennas, *Phys. Rev. Lett.* 102(14), 146807 (2009)
50. S. L. Chang, Multiple Diffraction of X-Rays in Crystals, Springer Series in Solid-State Sciences (SSSOL, Volume 50), Springer Berlin Heidelberg, 1984
51. S. C. Kitson, W. L. Barnes, and J. R. Sambles, Surface-plasmon energy gaps and photoluminescence, *Phys.*

*Rev. B* 52(15), 11441 (1995)
52. T. Iqbal, H. Tabassum, S. Afsheen, and M. Ijaz, Novel exposed and buried Au plasmonic grating as efficient sensors, *Waves Random Complex Media* 32(4), 1571 (2022)
53. S. Afsheen, A. Ahmad, T. Iqbal, M. Ijaz, and A. Bashir, Optimizing the sensing efficiency of plasmonic based gas sensor, *Plasmonics* 16(2), 541 (2021)
54. M. Javaid and T. Iqbal, Plasmonic bandgap in 1D metallic nanostructured devices, *Plasmonics* 11(1), 167 (2016)
55. P. Wang, D. J. Hu, Y. F. Xiao, and L. Pang, Suppression of metal grating to surface plasma radiation, *Acta Phys. Sin.* 64(8), 087301 (2015)
56. B. Wang, P. Yu, W. Wang, X. Zhang, H. C. Kuo, H. Xu, and Z. M. Wang, High-$Q$ plasmonic resonances: Fundamentals and applications, *Adv. Opt. Mater.* 9(7), 2001520 (2021)
57. S. Sun, H. T. Chen, W. J. Zheng, and G. Y. Guo, Dispersion relation, propagation length and mode conversion of surface plasmon polaritons in silver double-nanowire systems, *Opt. Express* 21(12), 14591 (2013)
58. H. Raether, Surface-Plasmons on Smooth and Rough Surfaces and on Gratings, Springer-Verlag, 1988
59. K. A. Willets and R. P. Van Duyne, Localized surface plasmon resonance spectroscopy and sensing, *Annu. Rev. Phys. Chem.* 58(1), 267 (2007)
60. W. Zhang, M. Caldarola, X. Lu, and M. Orrit, Plasmonic enhancement of two-photon-excited luminescence of single quantum dots by individual gold nanorods, *ACS Photonics* 5(7), 2960 (2018)
61. J. Wen, H. Wang, W. Wang, Z. Deng, C. Zhuang, Y. Zhang, F. Liu, J. She, J. Chen, H. Chen, S. Deng, and N. Xu, Room-temperature strong light–matter interaction with active control in single plasmonic nanorod coupled with two-dimensional atomic crystals, *Nano Lett.* 17(8), 4689 (2017)
62. T. A. Kelf, Y. Sugawara, R. M. Cole, J. J. Baumberg, M. E. Abdelsalam, S. Cintra, S. Mahajan, A. E. Russell, and P. N. Bartlett, Localized and delocalized plasmons in metallic nanovoids, *Phys. Rev. B* 74(24), 245415 (2006)
63. C. Belacel, B. Habert, F. Bigourdan, F. Marquier, J. P. Hugonin, S. Michaelis de Vasconcellos, X. Lafosse, L. Coolen, C. Schwob, C. Javaux, B. Dubertret, J. J. Greffet, P. Senellart, and A. Maitre, Controlling spontaneous emission with plasmonic optical patch antennas, *Nano Lett.* 13(4), 1516 (2013)
64. A. Agrawal, I. Kriegel, and D. J. Milliron, Shape-dependent field enhancement and plasmon resonance of oxide nanocrystals, *J. Phys. Chem. C* 119(11), 6227 (2015)
65. V. G. Kravets, A. V. Kabashin, W. L. Barnes, and A. N. Grigorenko, Plasmonic surface lattice resonances: A review of properties and applications, *Chem. Rev.* 118(12), 5912 (2018)
66. M. Ijaz, Plasmonic hot electrons: Potential candidates for improved photocatalytic hydrogen production, *Int. J. Hydrogen Energy* 48(26), 9609 (2023)
67. I. Boettcher, J. M. Pawlowski, and S. Diehl, Ultracold atoms and the functional renormalization group, *Nucl. Phys. B Proc. Suppl.* 228, 63 (2012)
68. H. Hertz, Ueber einen einfluss des ultravioletten lichtes auf die electrische entladung, *Ann. Phys.* 267(8), 983 (1887)
69. A. Einstein, Über einen die Erzeugung und verwandlung des lichtes betreffenden heuristischen gesichtspunkt, *Ann. Phys.* 322(6), 132 (1905)
70. M. L. Brongersma, N. J. Halas, and P. Nordlander, Plasmon-induced hot carrier science and technology, *Nat. Nanotechnol.* 10(1), 25 (2015)
71. Y. Dubi and Y. Sivan, "Hot" electrons in metallic nanostructures-non-thermal carriers or heating? *Light Sci. Appl.* 8(1), 89 (2019)
72. C. Clavero, Plasmon-induced hot-electron generation at nanoparticle/metal-oxide interfaces for photovoltaic and photocatalytic devices, *Nat. Photonics* 8(2), 95 (2014)
73. C. Sönnichsen, T. Franzl, T. Wilk, G. von Plessen, J. Feldmann, O. Wilson, and P. Mulvaney, Drastic reduction of plasmon damping in gold nanorods, *Phys. Rev. Lett.* 88(7), 077402 (2002)
74. J. B. Khurgin, Hot carriers generated by plasmons: Where are they generated and where do they go from there, *Faraday Discuss.* 214, 35 (2019)
75. J. B. Khurgin, Fundamental limits of hot carrier injection from metal in nanoplasmonics, *Nanophotonics* 9(2), 453 (2020)
76. R. Sundararaman, P. Narang, A. S. Jermyn, III Goddard, and H. A. Atwater, Theoretical predictions for hot-carrier generation from surface plasmon decay, *Nat. Commun.* 5(1), 5788 (2014)
77. M. M. Dujardin, and M. L. Theye, Investigation of the optical properties of Ag by means of thin semi-transparent films, *J. Phys. Chem. Solids* 32(9), 2033 (1971)
78. A. A. Maznev, and O. B. Wright, Demystifying umklapp vs normal scattering in lattice thermal conductivity, *Am. J. Phys.* 82(11), 1062 (2014)
79. G. R. Parkins, W. E. Lawrence, and R. W. Christy, Intraband optical conductivity σ(ω, T) of Cu, Ag, and Au: Contribution from electron-electron scattering, *Phys. Rev. B* 23(12), 6408 (1981)
80. U. Kreibig and M. Vollmer, Optical Properties of Metal Clusters, Vol. 25, Springer Berlin Heidelberg, 1995
81. L. Landau, On the vibrations of the electronic plasma, *Yad. Fiz.* 10, 25 (1946)
82. A. V. Uskov, I. E. Protsenko, N. A. Mortensen, and E. P. O'Reilly, Broadening of plasmonic resonance due to electron collisions with nanoparticle boundary: A quantum mechanical consideration, *Plasmonics* 9(1), 185 (2014)
83. J. B. Khurgin, Ultimate limit of field confinement by surface plasmon polaritons, *Faraday Discuss.* 178, 109 (2015)
84. J. Khurgin, W. Y. Tsai, D. P. Tsai, and G. Sun, Landau damping and limit to field confinement and enhancement in plasmonic dimers, *ACS Photonics* 4(11), 2871 (2017)
85. K. Watanabe, D. Menzel, N. Nilius, and H. J. Freund, Photochemistry on metal nanoparticles, *Chem. Rev.*

106(10), 4301 (2006)

86. N. S. Mueller, B. G. M. Vieira, D. Höing, F. Schulz, E. B. Barros, H. Lange, and S. Reich, Direct optical excitation of dark plasmons for hot electron generation, *Faraday Discuss.* 214, 159 (2019)
87. H. Inouye, K. Tanaka, I. Tanahashi, and K. Hirao, Ultrafast dynamics of nonequilibrium electrons in a gold nanoparticle system, *Phys. Rev. B* 57(18), 11334 (1998)
88. J. M. Ziman, Electrons and phonons: The theory of transport phenomena in solids, Oxford Classic Texts in the Physical Sciences, Clarendon Press, Oxford University Press, 2001
89. J. B. Khurgin and U. Levy, Generating hot carriers in plasmonic nanoparticles: When quantization does matter, *ACS Photonics* 7(3), 547 (2020)
90. T. P. White and K. R. Catchpole, Plasmon-enhanced internal photoemission for photovoltaics: Theoretical efficiency limits, *Appl. Phys. Lett.* 101(7), 073905 (2012)
91. J. Kadlec, Theory of internal photoemission in sandwich structures, *Phys. Rep.* 26(2), 69 (1976)
92. D. A. Kovacs, J. Winter, S. Meyer, A. Wucher, and D. Diesing, Photo and particle induced transport of excited carriers in thin film tunnel junctions, *Phys. Rev. B* 76(23), 235408 (2007)
93. S. V. Pepper, Optical analysis of photoemission, *J. Opt. Soc. Am.* 60(6), 805 (1970)
94. K. Reuter, U. Hohenester, P. L. de Andres, F. J. García-Vidal, F. Flores, K. Heinz, and P. Kocevar, Electron energy relaxation times from ballistic-electron-emission spectroscopy, *Phys. Rev. B* 61(7), 4522 (2000)
95. C. Scales and P. Berini, Thin-film Schottky barrier photodetector models, *IEEE J. Quantum Electron.* 46(5), 633 (2010)
96. S. Afsheen, T. Iqbal, S. Akram, A. Bashir, A. Tehseen, M. Rafique, M. Shakil, M. Y. Khan, and M. Ijaz, Surface plasmon based 1D-grating device for efficient sensing using noble metals, *Opt. Quantum Electron.* 52(2), 64 (2020)
97. T. Iqbal, A. Bashir, M. Shakil, S. Afsheen, A. Tehseen, M. Ijaz, and K. N. Riaz, Investigation of plasmonic bandgap for 1D exposed and buried metallic gratings, *Plasmonics* 14(2), 493 (2019)
98. Y. Takahashi and T. Tatsuma, Solid state photovoltaic cells based on localized surface plasmon-induced charge separation, *Appl. Phys. Lett.* 99(18), 182110 (2011)
99. C. Qiu, H. Zhang, C. Tian, X. Jin, Q. Song, L. Xu, M. Ijaz, R. J. Blaikie, and Q. Xu, Breaking bandgap limitation: Improved photosensitization in plasmonic-based $CsPbBr_3$ photodetectors via hot-electron injection, *Appl. Phys. Lett.* 122(24), 243502 (2023)
100. M. W. Knight, H. Sobhani, P. Nordlander, and N. J. Halas, Photodetection with active optical antennas, *Science* 332(6030), 702 (2011)
101. A. Di Bartolomeo, Graphene schottky diodes: An experimental review of the rectifying graphene/semiconductor heterojunction, *Phys. Rep.* 606, 1 (2016)
102. S. S. Li, Semiconductor Physical Electronics, New York, Springer, 2006
103. Y. Huan, S. M. Sun, C. J. Gu, W. J. Liu, S. J. Ding, H. Y. Yu, C. T. Xia, and D. W. Zhang, Recent advances in $\beta$-$Ga_2O_3$–metal contacts, *Nanoscale Res. Lett.* 13(1), 246 (2018)
104. S. J. Fonash, Solar Cell Device Physics, Elsevier, 2010